Scientific paper

Microscopic and Macroscopic Physical Properties of Meta-chert

Koki Maekawa[1], Wei Wang[2], Hamza Samouh[3], Shunsuke Ishikawa[4], Osamu Kontani[5], Takahiro Ohkubo[6], Kenta Murakami[7], Kiyoteru Suzuki[8], Ippei Maruyama[9,10*]

[1] Master Student, Graduate School of Environmental Studies, Nagoya University, Nagoya, Japan.
[2] Project appointed researcher, Graduate School of Engineering, The University of Tokyo, Tokyo, Japan.
[3]Project appointed researcher, Department of Civil and Environmental Engineering, University of Illinois at Urbana-Champaign.
[4] Engineer, Nuclear Power Department, Kajima Corporation, Tokyo, Japan.
[5] Principal Engineer, Nuclear Power Department, Kajima Corporation, Tokyo, Japan.
[6] Assoc. Prof., Graduate School of Engineering, Chiba University, Chiba, Japan.
[7] Assoc. Prof., Graduate School of Engineering, The University of Tokyo, Toyo, Japan.
[8] Research director, Societal Safety and Industrial Innovation Division, Mitsubishi Research Institute, Inc., Tokyo, Japan.
[9] Professor, Graduate School of Environmental Studies, Nagoya University, Nagoya, Japan.
[10] Professor, Graduate School of Environmental Studies, The University of Tokyo, Tokyo, Japan.
[*]Corresponding author, *E-mail:* i.maruyama@bme.arch.t.u-tokyo.ac.jp

Abstract

Herein, to determine the methods of obtaining various properties of aggregates, quartz-rich quartzite is selected, two types of different regions in aggregate, a region (white region) where quartz grains are densely compacted and another region (gray region) where quartz grains are secondarily formed coarsely, are tested for the linear expansion coefficient, and the tensile strength and Young's modulus. The microscopic data were compared with macroscopic data. Young's modulus is not significantly different between that of macroscopic compression and that of microscopic tension loading in the white region. Macroscopic splitting tensile strength shows bimodal behavior due to the failure mechanisms dominated by two different regions, which was experimentally confirmed by the data of the microscopic direct tensile loading test. The coefficients of thermal expansion of the macroscopic test are similar to that of the microscopic experiment for the white region, which is well reflected by the nature of quartz, on the contrary, the microscopic coefficient of thermal expansion of the gray region shows completely different behavior.

Keywords: Digital image correlation method; Coefficient of thermal expansion; Aggregate; Direct tensile test; Natural fracture.

1. Introduction

Nuclear power supply is defined as an important base-load electricity that is unable to utilize renewable energy efficiently (Ministry of energy trade and industry of Japan 2021); the long-term operation of nuclear power plants is one of the options for Japan's energy strategy. Therefore, aging management of concrete structures in nuclear power plants is a major research area. Concrete structural members in nuclear power plants are difficult to replace or incur considerable replacement cost; hence, evaluation methods for the soundness of concrete members in the current as well as in the future states are crucial. Neutron and gamma-ray irradiation environments are among the characteristic environments in nuclear power plants, and the impact of neutrons and gamma rays on concrete members is of concern (Kontani *et al.* 2010).

Previous studies have elucidated that neutron irradiation-induced volume expansion of rock-forming minerals in aggregates has a large influence on concrete degradation; additionally, the mechanical properties of concrete deterioration with no restraint state were well correlated with the expansion of the concrete (Elleuch *et al.* 1972; Hilsdorf *et al.* 1978; Maruyama *et al.* 2017). Therefore, the volume change in rock-forming minerals, as an input for the evaluation of concrete expansion due to radiation-induced volume expansion (RIVE), (Simon 1957; Primak 1958; Bates *et al.* 1974; Bykov *et al.* 1981; Douillard and Duraud 1996; Yuan *et al.* 2001; Mota *et al.* 2005; Denisov *et al.* 2012; Wang *et al.* 2015; Hsiao *et al.* 2017; Krishnan, Wang, Le Pape, *et al.* 2017; Krishnan, Wang, Yu, *et al.* 2017; Silva *et al.* 2018, 2022; Le Pape *et al.* 2020; Okada *et al.* 2020) as well as crack behavior through mineral grains and inter-grain boundaries (Elleuch *et al.* 1972; Hilsdorf *et al.* 1978; Denisov *et al.* 2012; Maruyama *et al.* 2017; Khmurovska and Štemberk 2021a, 2021b) are critical issues. However, data on aggregate properties at the scale of grains are scarce; this contributes to the development of constitutive laws for numerical calculations as well as validation of calculation results. Therefore, tensile and thermal expansion tests were conducted at the microscope scale.

In this study, meta-chert samples irradiated by neutrons and/or gamma rays elsewhere were tested to provide microscope-scale information under the conditions of heating and tensile loading.

2. Materials and methods

2.1 Materials

The rock used in this study was obtained from the Aichi Prefecture, Japan. The mineral composition identified by powder X-ray diffraction (XRD) and the chemical composition measured by X-ray fluorescence-based oxide composition are summarized in Table 1 and Table 2, respectively.

Based on a geological survey, the rock was identified as a meta-chert, whereas in our previous study (Maruyama *et al.* 2017), it was called a thermally altered tuff. In the following experiment, except for the compressive loading test, the specimens were obtained from a lump of this rock.

Table 1 Mineral composition (mass %) (Maruyama *et al.* 2017)

Mineral	Quartz	Albite	Anorthite	Anorthoclase	Orthoclase	Microcline	Biotite	Chlorite	Total
Mass %	91.85	0.77	2.3	0.61	0.5	3.03	0.44	0.5	100
1σ	1.92	0.21	0.58	0.4	0.4	0.63	0.7	0.27	

Table 2 Chemical composition (mass %) (Maruyama *et al.* 2017)

LOI	Chemical composition											
	SiO_2	Al_2O_3	Fe_2O_3	CaO	MgO	SO_3	Na_2O	K_2O	TiO_2	P_2O_5	MnO	Total
0.93	86.99	5.09	2.25	0.68	0.98	0.69	0.49	1.25	0.24	0.1	0.17	99.86

2.2 Macroscopic compression loading test

Specimens with a size of ∅45 mm × 90 mm cut from aggregates were used for compression test employing a universal testing machine (Matest, E161N). To confirm the accuracy of the testing machine, the standard test specimen was used for a trial in advance, and the results had a margin of error of ± 2.5%. Subsequently, the compressive strength and compressive Young's modulus were measured at a rate of 0.6 MPa/s for each specimen. Each reported value is the average of five replicates. Part of this experiment has been reported elsewhere (Maruyama *et al.* 2017).

2.3 Macroscopic splitting tensile strength test (Brazilian test)

Specimens with a size of ∅12 mm × 2 mm drilled and cut from aggregate lump were used for splitting tensile test loaded via a universal testing machine (Imada Seisakusyo, SV 201NA SH). The loading procedure was as follows. First, 20 N was loaded as an initial load to stabilize the disk specimen; subsequently, additional load was loaded at a rate of 0.6 MPa/s until the maximum load was achieved. The disk diameter and thickness were measured using a micrometer with a precision of 0.001 mm, and the splitting tensile strength of the specimens was calculated. Ten specimens were tested.

2.4 Microscopic tensile loading test

The tensile Young's modulus, tensile strength, and stress–strain behavior of very small aggregates that do not contain large faults or cracks were conducted on tiny specimens (2 × 10 × 0.5 mm^3). The tiny specimens were fabricated by core-drilling from a lump of rock with a diameter of 15 mm and then cut into rectangular shapes (2 mm × 10 mm) with a thickness of approximately 5 mm using a low-speed precision cutter (IsoMet, BUEHLER). Finally, tiny specimens (0.5-mm thickness) were obtained after polishing (#400, #1000, #2000, and #3000 grade). To control the cracking position during the loading experiment, notches (approximately

0.5 mm) were placed at the center of the specimens, as shown in Fig. 1. As there are two different regions (gray and white) in the meta-chert rock, as shown in Fig. 2, which might comprise minerals of different sizes, the specimens used for the tensile test were prepared based on the two regions separately. The dimensions of each specimen were measured using an image dimension measurement system (IM-8000, EYENCE Co.; precision: 0.1 μm), whereas the thickness of each specimen was measured using a micrometer (Mitutoyo, MDC-25SX; precision: 1 μm).

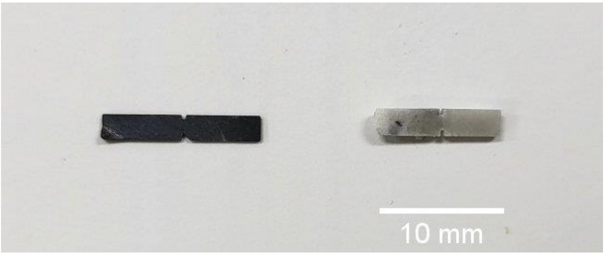

Fig. 1 Specimens for tensile loading

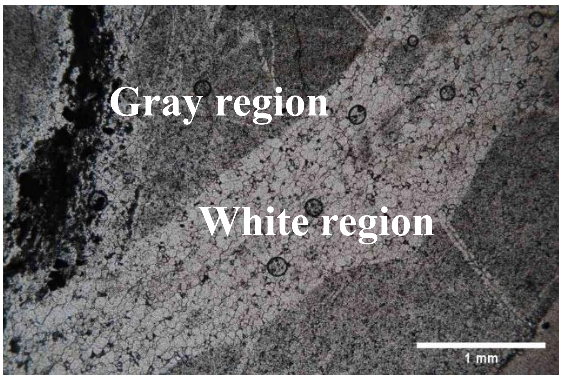

Fig. 2 Two distinct regions in aggregate

A micro-tension-compression testing device (Sanko, ISL-T3000) was used to conduct the tensile test (Fig. 3(a)). Both ends of the specimen were fixed using two newly designed jigs (Fig. 3(b)) and glue, and both jigs were attached to an actuator and a load cell. As the tensile behavior of the rock is dependent on the loading rate (Wu *et al.* 2015), the actuator of the device was set to the lowest speed (5 rpm) with a constant displacement rate of 2 μm/s to capture the micro-behavior of the aggregate. The corresponding value of the load cell was recorded every 200 ms, and the stress in the specimen was calculated by dividing the load by the cross-sectional area. Before formal loading, an initial compressive load (0.5 MPa) and tensile load (1.5 MPa) were applied to the specimens to ensure that they were placed well.

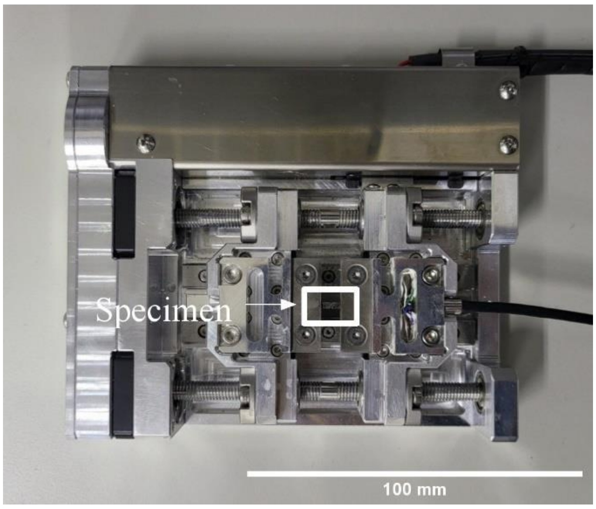

(a) Micro-tension-compression device with the specimen

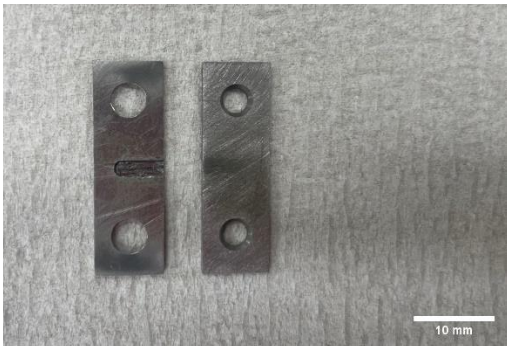

(b) Newly designed jigs for rock specimen

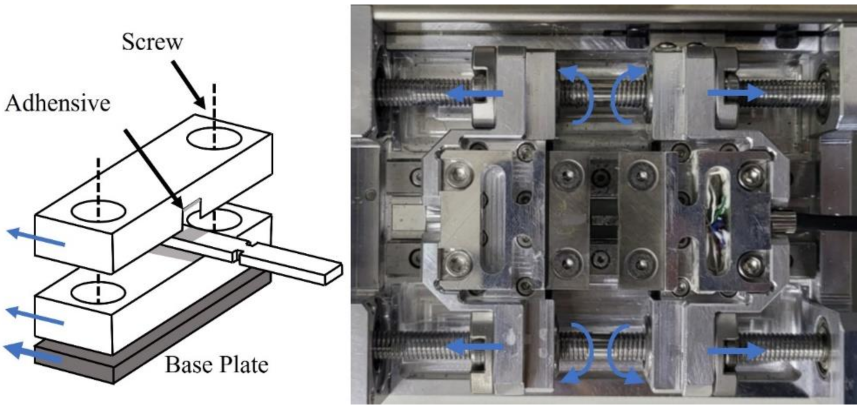

(c) Schematic of test apparatus

(d) Overall set-up of tensile loading experiment

Fig. 3 Tensile test of tiny aggregate specimens

Because the deformation of the adhesive glue between the jig and specimen was large, the deformation obtained from the displacement sensors would be imprecise. Therefore, the digital image correlation method (DICM) was used with a charge-coupled device camera (GS3-U3-51S, FLIR, resolution: 5M pixels) installed on the microscope. The exposure time was 7 ms for each image, and the interval was consistent with the loading measurement time (200 ms). The total number of images per loading test was approximately 1000. The software Vic-2D (Correlated Solutions Inc.) was used to analyze the images. Fig. 4 shows the target analysis area, which is green in the picture, and the detailed setting is summarized in Table 3.

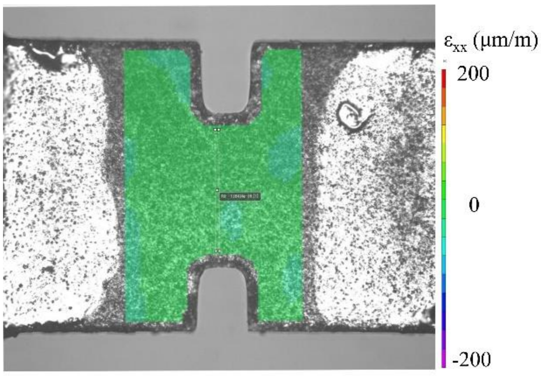

Fig. 4 Target area of DICM in the specimen

Table 3 Setting parameters used in DICM

Subset	89
Steps	24
Subset weights	Gaussian weights
Interpolation	Optimized 6-tap
Criterion	Normalized squared differences
Exhaustice search	On
Consistency threshold maximum margin	0.02 pixel
Confidence margin maximum margin	0.02 pixel
Matchability threshold maximum margin	0.10 pixel

Several methods can be used to calculate the strain from DICM. To precisely obtain the strain, a comparison was made between the ε_{xx} strain and extensometer methods. The ε_{xx}-strain method uses the average strain value parallel to the loading direction for all pixels in the selected area, whereas the extensometer method uses the average calculated value of the displacement between two points in 17 vertically divided parts of the same selected area. As shown in Fig. 5, although the overall stress–strain relation exhibits a similar trend in both cases, the ε_{xx} strain is more convergent and can be fitted well within the elastic range. Therefore, the

ε_{xx} strain was used in this study.

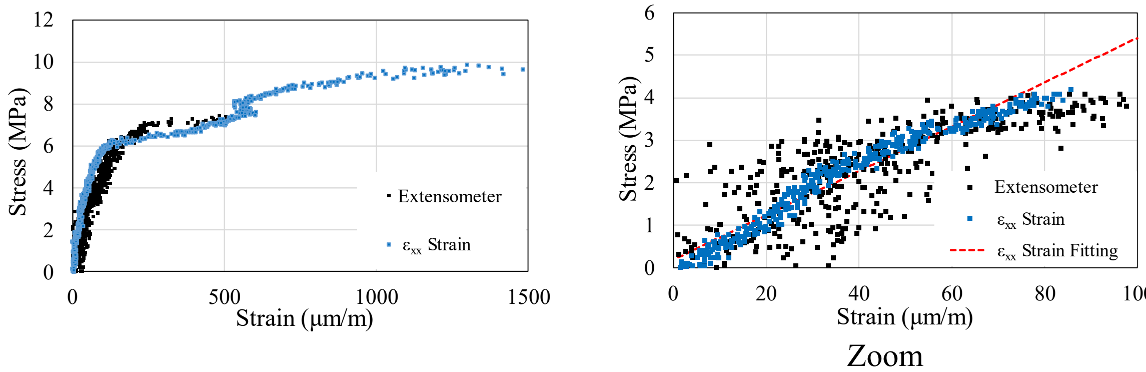

Fig. 5 Comparison between ε_{xx} strain and exotensometer

In addition, to determine the value of the subset, the strain was calculated with subsets 49, 59, 69, 79 and 89, and the corresponding stress–strain curves are shown in Fig. 6. As the stress–strain curve with subset 89 converged sufficiently to confirm linearity, this value was used in the following analysis. Furthermore, the strains with large deviations were removed using a median filter. Based on the obtained stress–strain curves, the Young's modulus of the specimens was calculated through linear approximation fitting of the curves within the elastic range (<50 μm).

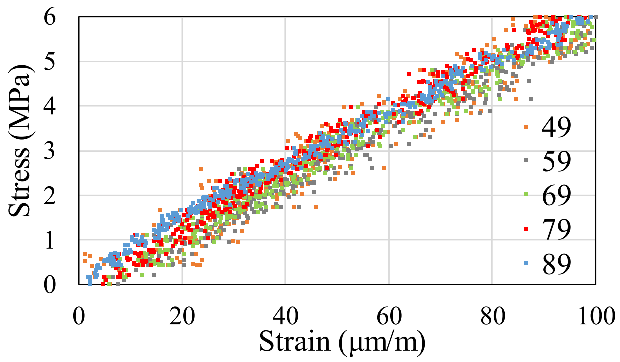

Fig. 6 Stress–strain curves with different subsets

2.5 Macro- and micro-scale measurements of the coefficient of thermal expansion

Six cylindrical specimens with dimensions of Φ10 mm × 10 mm were prepared from the rock to measure the macro-scale coefficient of thermal expansion (CTE) using a thermomechanical analyzer (SHIMAZU Corporation, TMA-60HS). A rate of 1 °C/min was selected and a 5-N force was applied to the center of the specimen to maintain stability during the measurement.

In addition, a part of the rock was cut and glued to rectangular glass and then polished until a thickness of 30 μm was achieved. Subsequently, a polarizing microscope was used to identify the shapes and sizes of the minerals under cross-polarized light (XPL) and plane-polarized light

(PPL) at 400× magnification. The micro-scale CTE was measured using the same specimens for the polarizing microscope with the heating stage (PN121-D, MSA Factory Co., Ltd.), which can regulate the temperature through its monitor. The heating stage had a small hole at its center and a glass cover to protect the micrograph lens, and the maximum temperature was 200 °C. As shown in Fig. 7(a), both sides of the specimen were fixed to a glass cover with double-sided tape. Thereafter, the temperature was increased from 25 °C to 100 °C at intervals of 5 °C at a rate of 1 °C/min; additionally, one image was captured at each interval. Considering the temperature distribution, images were captured after 1 min of each target temperature interval to ensure that the specimens reached the same temperature as the hotplate. Similarly, the DICM method with Vic-2D was used to measure and analyze the strain of the specimens with settings similar to those in Section 2.3. For the strain analysis, three rectangular areas were selected for the gray and white regions, as shown in Fig. 7(b); subsequently, the averaged e_{xx}/e_{yy} strain was obtained. Finally, the linear expansion coefficient was calculated based on the strain curves with respect to the temperature.

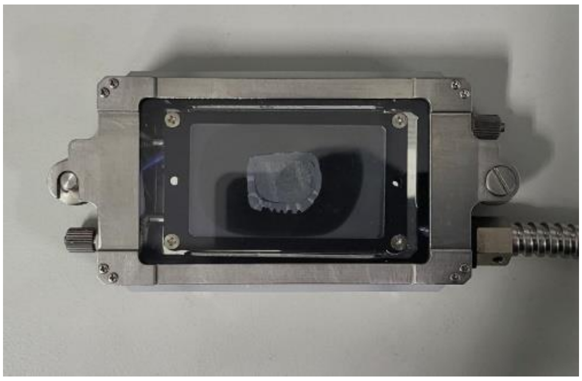

(a) Heating stage

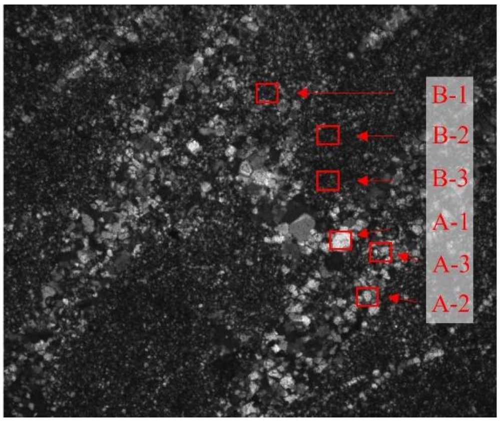

(b) Image taken by a polarizing microscope (50×) and area selected for analysis

Fig. 7 Micro-CTE measurement set-up and selected analysis areas

3. Experimental results

3.1 Macroscopic compression and tensile test

The compressive strength was 56 ± 5.0 MPa and compressive Young's modulus of the specimens was 74 ± 15 GPa.

The splitting tensile strengths of the disk-shaped specimens are shown in Fig. 8. The average strength was 11.9 MPa, and the standard error was 6.7 MPa. The minimum value was 3.7 MPa, and the maximum value are 20.9 MPa.

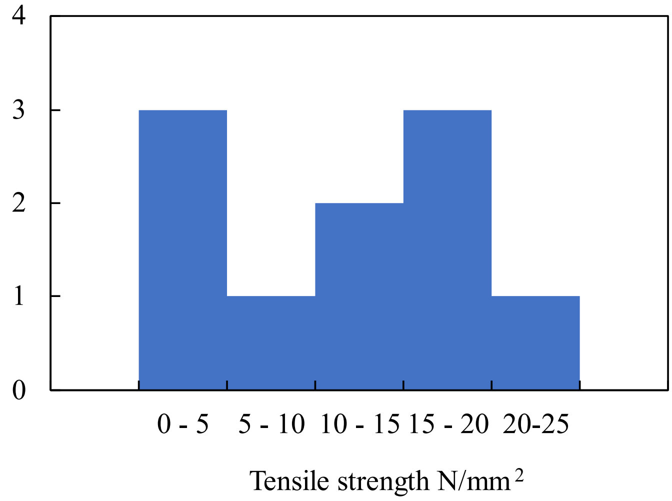

Fig. 8 Histogram of splitting tensile strength test

3.2 Microscopic tensile loading test

The stress–strain curves, tensile strength, and tensile Young's modulus of the two distinct regions are presented in Fig. 9 and Table 4, respectively. Here, MC1 represents the specimens taken from the white region of the rock, whereas MC2 represents the gray region. The tensile strength of the gray region specimen was approximately twice that of the white region specimen, whereas the Young's modulus of the gray region was approximately four times that of the white region.

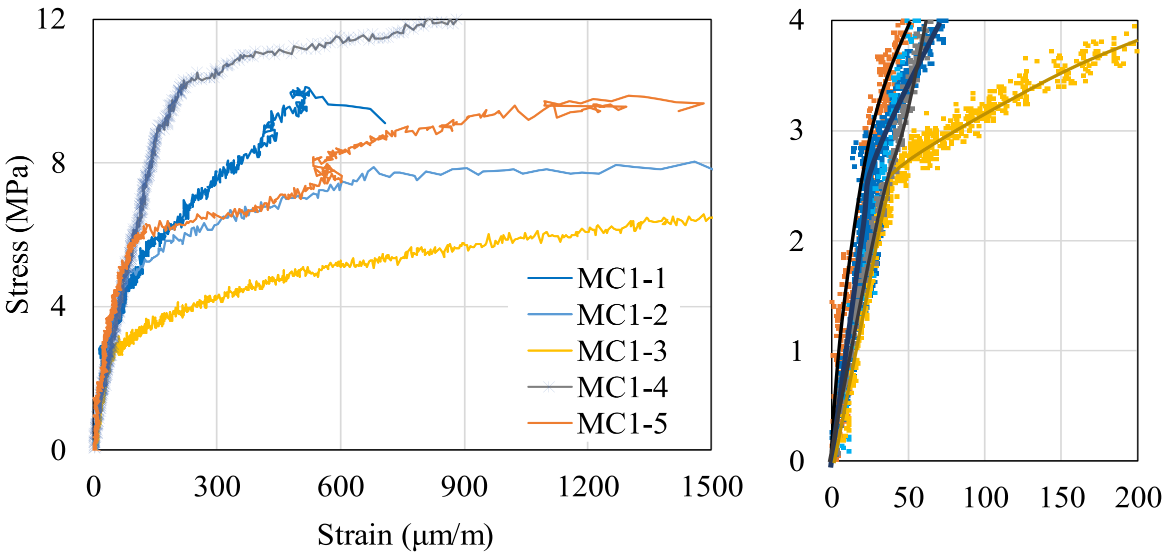

(a) Gray region specimens

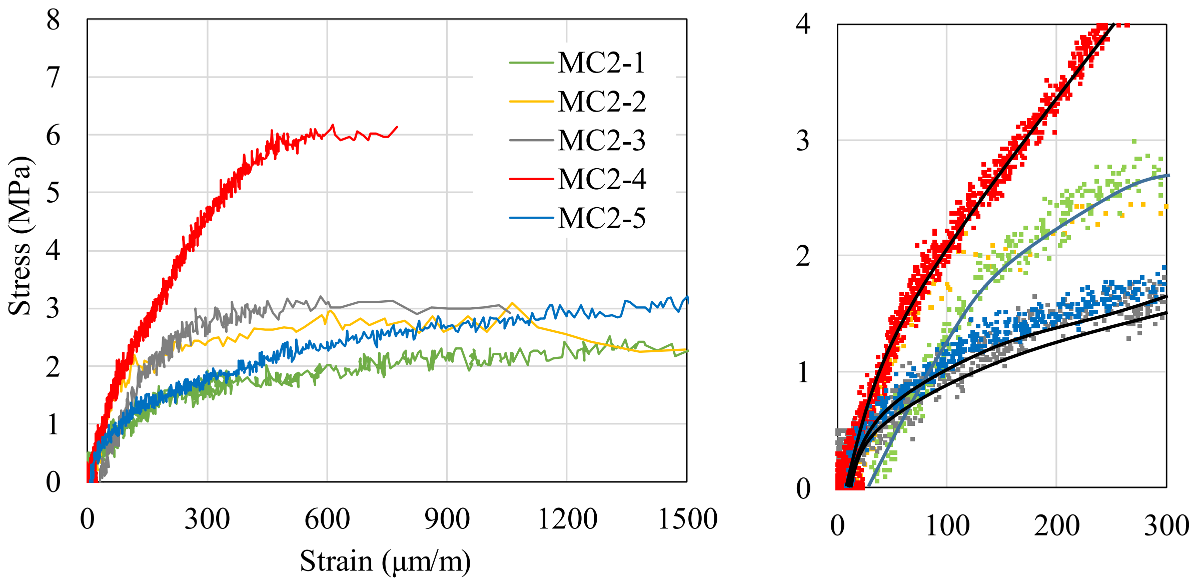

(b) White region specimen

Fig. 9 Stress–strain curves relative to direct tensile test

Table 4 Microscopic tensile loading test results

	Tensile strength (MPa)	Young's modulus (GPa)
MC1 Gray region, small grains densely packed	9.6 ± 2.7	62 ± 5.0
MC2 White region, Large grains coarsely packed	4.1 ± 2.2	17 ± 10.4

Fig. 10 shows the development of the strain fields of the specimens during the tensile test; evidently, the strain increased from the edge to the center of the specimen. As the development of the strain field in the white and gray specimens was almost the same, only one example is provided here. At 50 s, the strain of all specimens was still very low. At 120 s, the strain at the edge of the specimen exceeded 2×10^{-4}. When the time continued to increase from 120 s to 200 s, the strain spread from the edge to the center of the specimen and exceeded 5×10^{-4}, as well as some small cracks occurred at the edge and propagated to the center of the specimens. Subsequently, the specimens failed. This implies that when the specimen was subjected to tensile loading, the strain initially generated at the edge of the specimen and distributed to the center; after a certain point, cracking at the edge of the specimen led to the final damage of the specimen.

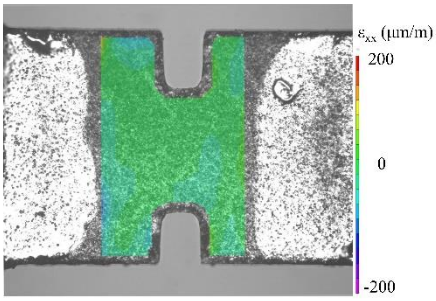

(b) 50 s

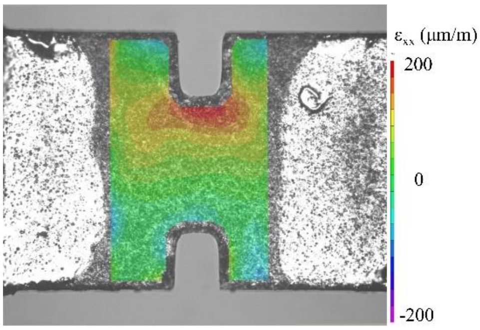

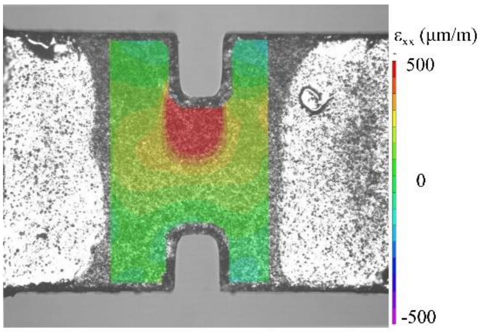

(c) 120 s (d) 200 s

Fig. 10 Strain field of specimens during tensile test

3.3 Macro-scale coefficient of thermal expansion

The temperature–strain curves and macro-CTEs of the specimens in the three directions are presented in Fig. 11 and Table 5, respectively. The CTEs in the Y- and Z-axes were almost the same, and the TEC in the X-axis was smaller than those in the Y- and Z-axes, which is similar to the trend exhibited by pure quartz (c-axis: 0.78×10^{-5} /°C, and a-, b-axes: 1.44×10^{-5}/°C). This similarity in the trend may be owing to the high quartz content in the specimens (Rosenholtz and Smith 1941).

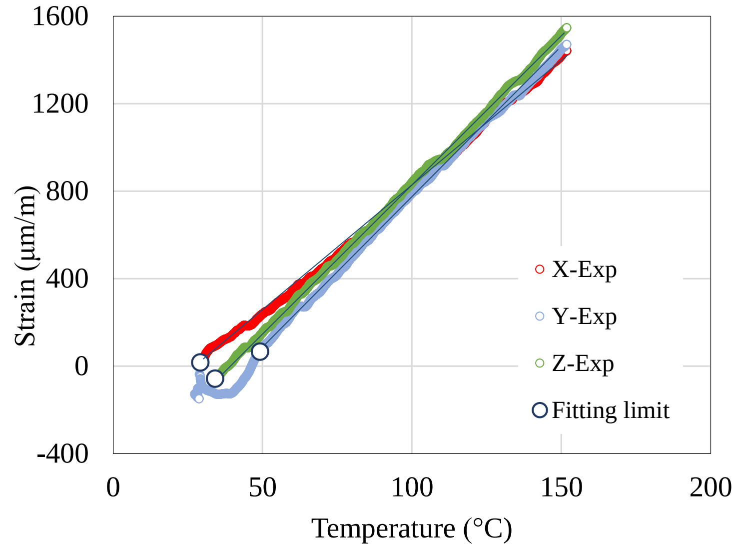

Fig. 11 Strain of quartzite according to different directions versus the temperature

Table 5 Measured CTE for quartzite based on different directions

Direction	CTE 10^{-6}/°C
X	11.6
Y	13.6
Z	13.5

3.4 Micro-scale coefficient of thermal expansion

Polarized micrographs are shown in Fig. 12; they suggest that the minerals in the meta-chat were composed primarily of quartz with different sizes and shapes. This is shown in Fig. 7(b). Micro-CTE measurements were conducted in two types of areas. Area A represents a group of minerals with large grain sizes, whereas area B represents minerals with small grain sizes. This corresponds to the classification applied in the microscopic tensile loading test, where the white region comprises large minerals, whereas the gray region comprises small minerals.

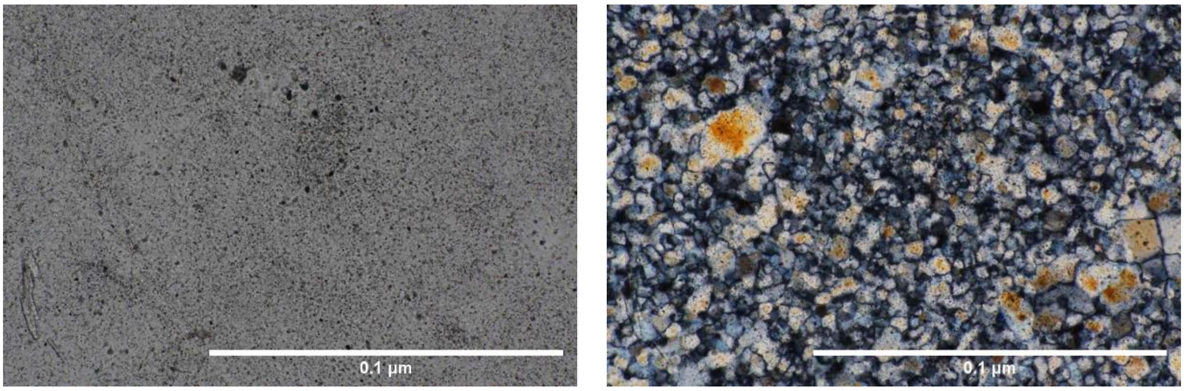

PPL XPL

Fig. 12 Polarized micrographs of meta-chert samples

The temperature–strain curves and micro-CTEs of the selected areas are presented in Fig. 13 and Table 6, respectively. Compared with the strain of the B-type areas, the strain of the A-type areas was unstable and not constant, and different temperature–strain curves were obtained at different locations. To further investigate the reason behind this type of instability, the strain between the two points in the A-type area was measured by deviating the angle by 45°, as shown in Fig. 14, and the deformation behavior was elliptical. For example, in the case of A-1, a positive strain (tensile direction) occurred at 45° and 90°, whereas a negative strain (compression direction) occurred at 135°.

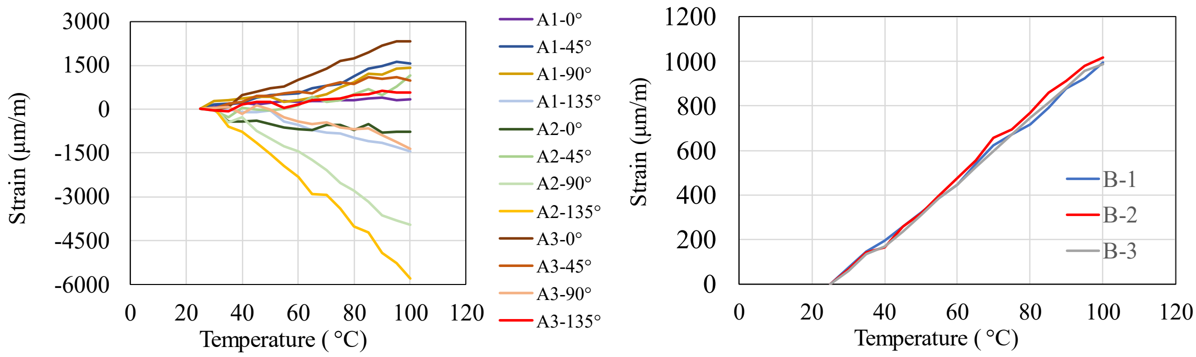

(a) A-type (large grains coarsely packed like white region)

(b) B-type (small grains densely packed like gray region)

Fig. 13 Strain of selected areas versus the temperature

Table 6 CTE of B-type areas

	CTE 10^{-6}/°C	
	ε_{xx}	ε_{yy}
B-1	13.3	14.4
B-2	14.2	14.1
B-3	13.7	11.6
Average	13.7	13.4

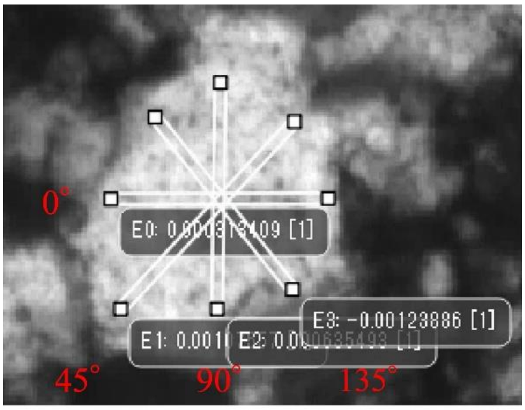

Fig. 14 Strain measurement points in A-type area (large grain size, like white region)

4. Discussion

4.1 Mechanical behavior of aggregate about compression and tensile stress

Owing to the difficulty in preparing the specimens and natural fractures in the rocks, research on the tensile behavior of rocks is limited; to the best of our knowledge, research on the difference in the tensile behavior and compressive behavior of aggregates is lacking.

First, Young's modulus in compression and tension was discussed. The macroscopic compressive Young's modulus was 74 GPa, whereas the microscopic tensile Young's moduli were 62 GPa for the gray region (small grains and densely packed) and 17 GPa for the white region (large grains and coarsely packed). A large number of cracks were observed in the aggregate lumps. During compressive loading, these cracks were closed and could transfer the stress, whereas they were difficult to tension. In the microscopic experiment, these cracks were avoided to prepare sound specimens. However, the specimens were prepared such that an impact of voids and fine cracks on the tensile Young's modulus was still observed. Therefore, in both cases, Young's modulus under tension was smaller than that under compression. The detailed textures of the gray and white regions are shown in Fig. 15. In the white region, large quartz grains were coarsely re-precipitated in a vain and had large pores. Based on this figure, the low Young's modulus can be easily explained.

The stress–strain curves exhibited a monotonic decrease in stiffness, as shown in Fig. 9. This trend can be explained by the increase in the number of defects and fine cracks as well as the continuous crack opening (Hawkes *et al.* 1973). In the current experiments, as shown in Fig. 10, it was generally one of the sides of the notch, thus exhibiting a larger strain increase than that of the other notch side. This indicates a gradual crack opening from one side to the other, which could be the reason for nonlinear stress development.

The splitting tensile strength of the disk specimens was 11.9 MPa, whereas the direct tensile strength was approximately 4.1 MPa (white region, large quartz grains coarsely packed) and approximately 9.6 MPa (gray region, small quartz grains densely packed). The splitting tensile strength presented bimodal results, as shown in Fig. 8. This result was consistent with the fact that the aggregates contains two distinct regions; moreover, it reflects that each region has inherent strength. However, the splitting tensile strength overestimates the direct tensile strength, as reported by numerous researchers (Li and Wong 2013). The discrepancy between the splitting tensile strength and microscopic direct tensile strength can be explained by the stress development and resultant defect creation process in the specimen, as follows. In the case of the splitting tensile strength, horizontal tensile stress occurs during vertical loading. Owing to the large area of the section, even if defects are created, other stress paths exist in the middle part of the specimen. Therefore, the result was reflected by the average specimen texture. In the case of microscopic direct tensile loading, the impact of one defect is more pronounced and a crack develops easily, starting from the defect to across the specimen; this crack breaks the specimen rapidly. Therefore, the microscopic direct tensile loading result is well reflected by the local strength of concrete, and the Brazilian test cannot provide local strength information.

The tensile strength of the white region was lower than those of the gray specimens. As shown in Fig. 15, their structures were different, and numerous defects existed in the white specimens. Combined with natural fractures, such a defect area can hardly bear any tensile stress; consequently, the tensile strength of the specimens decreased with the number and size of the defected areas.

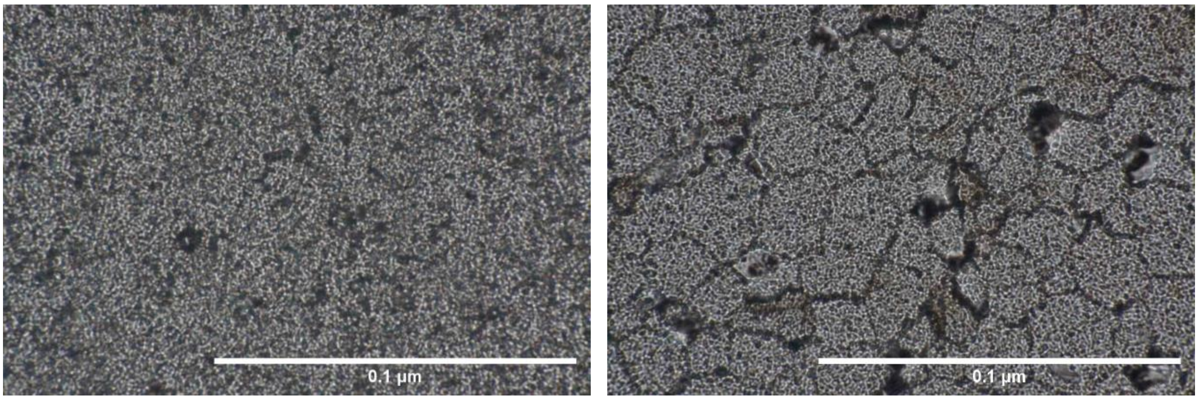

(a) Gray-region based specimen (b) White-region based specimen

Fig. 15 Micrographs of specimens taken with a polarized microscope at 400×.

4.2 Comparison of the results of two types of experiments on CTE

Generally, rocks are composed of several minerals, and their thermal expansion is anisotropic. Considering the different atomic structures, the orthorhombic, monoclinic, and triclinic crystal systems have different CTEs in three directions. In this case, the thermal expansion of minerals composed of these systems was anisotropic. Furthermore, quartz is considered to have considerable influence on the thermal expansion of rocks owing to its high-temperature sensitivity and anisotropic expansion (Johnson and Parsons 1944; Igarashi *et al.* 2015).

The macro-CTEs of the specimens in this study were different in the x-, y-, and z-directions. Compared with the macro-CTE, the micro-CTE was slightly larger, and the average values in the x and y directions were similar to those in the y and z directions, as presented in Tables 6 and 7. The CTE of the pure quartz was larger than that of the specimens used in this study(Rosenholtz and Smith 1941). The difference in the CTE of minerals and aggregates depends not only on the texture but also on the natural fractures and stress. Compared with the specimens with small quartz grains, the strain of the specimens with large quartz grains was not stable. Under a polarizing microscope (400×), black streaks at the boundaries of the large quartz grains were observed, as shown in Fig. 12. With regard to the quartz grains, the small quartz grains were densely bonded and almost no boundaries could be observed, whereas the large quartz grains had a boundary area of approximately 0.003 mm. Therefore, the small quartz grains were not affected by defects and expanded the same way in all areas, whereas the large quartz grains were affected by the large size of the quartz grains and the boundaries or defects that existed around them. These results indicate that local stress can be produced in the aggregate owing to the inhomogeneous contacts around the grains, which may also influence the fracture process of the aggregate.

5. Conclusion

The macroscopic compressive Young's modulus and splitting tensile strength were compared with the microscopic tensile Young's modulus, and the direct tensile strength of two different characteristic regions of the aggregate were compared. In general, the compressive Young's modulus is larger than that in tension; this can be explained by the originally existing defects and cracks, which can transfer the compressive stress and cannot transfer the tensile stress. The macroscopic splitting tensile strength was greater than the local direct tensile strength. This is due to the difference in crack development and resultant loading path creation after crack development. A microscopic direct tensile loading experiment can detect the local strength, which is well reflected by the grain-based texture.

The macroscopic and microscopic thermal expansion coefficients were sometimes very consistent, particularly when the quartz grains were densely packed; in contrast, the trend was different in the region where large grains were coarsely packed. The inhomogeneous contact of grains causes different stress fields and results in completely different thermal deformation behaviors. Therefore, the local stress, which has a large influence on the crack development, is determined by the local grain-based texture. This information should contribute to the understanding of physical property changes due to alternation, such as neutron irradiation-induced volume expansion of minerals.

Acknowledgements

Part of this study is the result of the "Japan Concrete Aging Management Program on Irradiation

Effects (JCAMP)," sponsored by the Ministry of Economy, Trade, and Industry (METI) in Japan.

Conflicts of Interest

The authors declare no conflict of interest.

CRediT author statement

KM: Formal analysis, Investigation, Writing - original draft

WW: Investigation, Writing - original draft, Writing - review & editing

HS: Methodology, Writing - review & editing

DK: Methodology, Writing - review & editing

OK: Funding acquisition, Methodology, Writing - review & editing

SI: Methodology, Writing - review & editing

TO: Methodology, Writing - review & editing

KM: Methodology, Writing - review & editing

KS: Funding acquisition, Project administration, Writing - review & editing

IM: Project administration, Conceptualization, Resources, Methodology, Funding acquisition, Supervision, Formal analysis, Writing - original draft, Writing - review & editing

References

Bates, J. B., Hendricks, R. W. and Shatter, L. B., (1974). "Neutron irradiation effects and structure of noncrystalline SiO2." *The Journal of Chemical Physics*, 61 (10), 4163-4176, doi: 10.1063/1.1681714.

Bykov, V. N., Denisov, A. V, Dubrovskii, V. B., Korenevskii, V. V, Krivokoneva, G. K. and Muzalevskii, L. P., (1981). "Effect of irradiation temperature on the radiation expansion of quartz." *Soviet Atomic Energy*. Kluwer Academic Publishers-Plenum Publishers, 51 (3), 593-595, doi: 10.1007/BF01135758.

Denisov, A., Dubrovskii, V. and Solovyov, V., (2012). "*Radiation resistance of mineral and polymer construction materials*." ZAO MEI Publishing House.

Douillard, L. and Duraud, J. P., (1996). "Amorphization of α-quartz under irradiation." *Journal de Physique III*, 6 (12), 1677-1687.

Elleuch, L. F., Dubois, F. and Rappeneau, J., (1972). "Effects of Neutron Radiation on Special Concretes and Their Components." *Special Publication*, 34, doi: 10.14359/18107.

Hawkes, I., Mellor, M. and Gariepy, S., (1973). "Deformation of rocks under uniaxial tension." *International Journal of Rock Mechanics and Mining Sciences and*, 10 (6), 493-507, doi: 10.1016/0148-9062(73)90001-6.

Hilsdorf, H., Kropp, J. and Koch, H., (1978). "The effects of nuclear radiation on the mechanical properties of concrete." *ACI SP-55*, 223-251.

Hsiao, Y. H., La Plante, E. C., Krishnan, N. M. A., Le Pape, Y., Neithalath, N., Bauchy, M.

and Sant, G., (2017). "Effects of Irradiation on Albite's Chemical Durability." *Journal of Physical Chemistry A*. American Chemical Society, 121 (41), 7835-7845, doi: 10.1021/acs.jpca.7b05098.

Igarashi, G., Maruyama, I., Nishioka, Y. and Yoshida, H., (2015). "Influence of mineral composition of siliceous rock on its volume change." *Construction and Building Materials*. Elsevier Ltd, 94, 701-709, doi: 10.1016/j.conbuildmat.2015.07.071.

Johnson, W. H. and Parsons, W. H., (1944). "Thermal expansion of concrete aggregate materials." *Journal of Research of the National Bureau of Standards*, 32 (3), 101, doi: 10.6028/jres.032.002.

Khmurovska, Y. and Štemberk, P., (2021a). "Catalogue of Radiation-Induced Damage of Rock Aggregates Identified by RBSM Analysis." *Journal of Advanced Concrete Technology*. Japan Concrete Institute, 19 (6), 668-686, doi: 10.3151/JACT.19.668.

Khmurovska, Y. and Štemberk, P., (2021b). "RBSM-based model for prediction of radiation-induced volumetric expansion of concrete aggregates." *Construction and Building Materials*. Elsevier, 294, 123553, doi: 10.1016/J.CONBUILDMAT.2021.123553.

Kontani, O., Ichikawa, Y., Ishizawa, A., Takizawa, M. and Sato, O., (2010). "Irradiation effects on concrete structure." *International Symposium on the Ageing Management of Nuclear Power Plants*, 173-182.

Krishnan, N. M. A., Wang, B., Le Pape, Y., Sant, G. and Bauchy, M., (2017). "Irradiation- vs. vitrification-induced disordering: The case of α -quartz and glassy silica." *Journal of Chemical Physics*. American Institute of Physics Inc., 146 (20), 204502, doi: 10.1063/1.4982944.

Krishnan, N. M. A., Wang, B., Yu, Y., Le Pape, Y., Sant, G. and Bauchy, M., (2017). "Enthalpy landscape dictates the irradiation-induced disordering of quartz.",*Physical Review X. American Physical Society*, 7 (3), 031019, doi: 10.1103/PhysRevX.7.031019.

Li, D. and Wong, L. N. Y., (2013). "The brazilian disc test for rock mechanics applications: Review and new insights." *Rock Mechanics and Rock Engineering*, 46 (2), 269-287, doi: 10.1007/s00603-012-0257-7.

Maruyama, I., Kontani, O., Takizawa, M., Sawada, S., Ishikawa, S., Yasukouchi, J., Sato, O., Etoh, J. and Igari, T., (2017). "Development of soundness assessment procedure for concrete members affected by neutron and gamma-ray irradiation." *Journal of Advanced Concrete Technology*, 15 (9), 440-523, doi: 10.3151/jact.15.440.

Ministry energy trade and industry of Japan, (2021). "*Outline of Strategic Energy Plan Agency for Natural Resources and Energy*.".

Mota, F., Caturla, M. J., Perlado, J. M., Dominguez, E. and Kubota, A., (2005). "Threshold energy of formation of an oxygen vacancy defect in SiO 2 by atomic displacements using molecular dynamics." *Fusion Engineering and Design*, 75–79(SUPPL.), 1027-1030, doi: 10.1016/j.fusengdes.2005.06.215.

Okada, N., Ohkubo, T., Maruyama, I., Murakami, K. and Suzuki, K., (2020). "Characterization of irradiation-induced novel voids in α -quartz." *AIP Advances*. AIP Publishing LLCAIP Publishing, 10 (12), 125212, doi: 10.1063/5.0029299.

Le Pape, Y., Sanahuja, J. and Alsaid, M. H. F., (2020). "Irradiation-induced damage in concrete-forming aggregates: revisiting literature data through micromechanics." *Materials and Structures/Materiaux et Constructions*. Springer Netherlands, 53 (3), 1-35, doi: 10.1617/s11527-020-01489-6.

Primak, W., (1958). "Fast-neutron-induced changes in quartz and vitreous silica." *Physical Review*, 110 (6), 1240-1254, doi: 10.1103/PhysRev.110.1240.

Rosenholtz, J. L. and Smith, D. T., (1941). "Linear thermal expansion and inversions of quartz, var. rock crystal." *American Mineralogist*, 26 (2), 103-109.

Silva, C. M., Rosseel, T. M. and Holliday, K. S., (2022). "Radiation-Induced Changes in Single Crystal Calcite and Dolomite: Mineral Analogues of Light Water Reactor, Nuclear Power Plant Concrete Aggregates." *Journal of Physical Chemistry C*. American Chemical Society, 126 (1), 634-646, doi: 10.1021/ACS.JPCC.1C08567/SUPPL_FILE/JP1C08567_SI_002.PDF.

Silva, C. M., Rosseel, T. M. and Kirkegaard, M. C., (2018). "Radiation-Induced Changes in Quartz, A Mineral Analog of Nuclear Power Plant Concrete Aggregates." *Inorganic Chemistry*. American Chemical Society, 57 (6), 3329-3338, doi: 10.1021/acs.inorgchem.8b00096.

Simon, I., (1957). "Structure of Neutron-Irradiated Quartz and Vitreous Silica." *Journal of the American Ceramic Society*. John Wiley & Sons, Ltd, 40 (5), 150-153, doi: 10.1111/J.1151-2916.1957.TB12593.X.

Wang, B., Yu, Y., Pignatelli, I., Sant, G. and Bauchy, M., (2015). "Nature of radiation-induced defects in quartz." *The Journal of Chemical Physics*. AIP Publishing LLCAIP Publishing, 143 (2), 024505, doi: 10.1063/1.4926527.

Wu, B., Chen, R. and Xia, K., (2015). "Dynamic tensile failure of rocks under static pre-tension." *International Journal of Rock Mechanics and Mining Sciences*. Elsevier, 80, 12-18, doi: 10.1016/j.ijrmms.2015.09.003.

Yuan, X., Pulim, V. and Hobbs, L. W., (2001). "Molecular dynamics refinement of topologically generated reconstructions of simulated irradiation cascades in silica networks." *Journal of Nuclear Materials*, 289 (1–2), 71-79, doi: 10.1016/S0022-3115(00)00703-0.